Local characteristics of the nocturnal boundary layer in response to external pressure forcing

van der Linden, Steven J.A.; Baas, Peter; van Hooft, J. Antoon; van Hooijdonk, Ivo G.S.; Bosveld, Fred C.; van de Wiel, Bas J.H.

Citation (APA)
van der Linden, S. J. A., Baas, P., van Hooft, J. A., van Hooijdonk, I. G. S., Bosveld, F. C., & van de Wiel, B. J. H. (2017). Local characteristics of the nocturnal boundary layer in response to external pressure forcing. *Journal of Applied Meteorology and Climatology*, *56*(11), 3035-3047. https://doi.org/10.1175/JAMC-D-17-0011.1

Important note
To cite this publication, please use the final published version (if applicable).
Please check the document version above.

Local Characteristics of the Nocturnal Boundary Layer in Response to External Pressure Forcing

STEVEN J. A. VAN DER LINDEN, PETER BAAS, AND J. ANTOON VAN HOOFT

Geoscience and Remote Sensing, Delft University of Technology, Delft, Netherlands

IVO G. S. VAN HOOIJDONK

Fluid Dynamics Laboratory and J. M. Burgers Center, Eindhoven University of Technology, Eindhoven, Netherlands

FRED C. BOSVELD

Royal Netherlands Meteorological Institute, De Bilt, Netherlands

BAS J. H. VAN DE WIEL

Geoscience and Remote Sensing, Delft University of Technology, Delft, Netherlands

ABSTRACT

Geostrophic wind speed data, derived from pressure observations, are used in combination with tower measurements to investigate the nocturnal stable boundary layer at Cabauw, the Netherlands. Since the geostrophic wind speed is not directly influenced by local nocturnal stability, it may be regarded as an external forcing parameter of the nocturnal stable boundary layer. This is in contrast to local parameters such as in situ wind speed, the Monin–Obukhov stability parameter (z/L), or the local Richardson number. To characterize the stable boundary layer, ensemble averages of clear-sky nights with similar geostrophic wind speeds are formed. In this manner, the mean dynamical behavior of near-surface turbulent characteristics and composite profiles of wind and temperature are systematically investigated. The classification is found to result in a gradual ordering of the diagnosed variables in terms of the geostrophic wind speed. In an ensemble sense the transition from the weakly stable to very stable boundary layer is more gradual than expected. Interestingly, for very weak geostrophic winds, turbulent activity is found to be negligibly small while the resulting boundary cooling stays finite. Realistic numerical simulations for those cases should therefore have a comprehensive description of other thermodynamic processes such as soil heat conduction and radiative transfer.

1. Introduction

In this paper, a climatology of 11 yr of observations of the nocturnal boundary layer (NBL) is presented in terms of geostrophic wind speed. As we will focus on clear-sky cases only, mechanical forcing is expected to be the major factor determining the evolution of the NBL. For offline numerical studies of the NBL, for example, using single-column models or large-eddy simulations (LESs), the geostrophic wind is often taken as an a priori known *external* parameter that is

either available from large-scale numerical weather prediction (NWP) output or specifically chosen.

By contrast, from an observational perspective the NBL is often characterized by relations among *local, internal parameters* such as the local gradient Richardson number Ri or the ratio of observation height to the Obukhov length z/L. By internal, we mean that these parameters are not known a priori but rather are the result of the boundary layer's response to external forcing and local surface characteristics. As probing of the NBL is generally done by measuring vertical profiles of, for example, wind speed and air temperature along a single tower, it is natural to investigate turbulent characteristics in relation to these parameters. These approaches have led to many valuable insights into the structure of

Corresponding author: S. J. A. van der Linden, s.j.a.vanderlinden@tudelft.nl

the stable boundary layer in response to increasing stability (see, e.g., Mahrt 1998; Grachev et al. 2005; Mauritsen and Svensson 2007; Zilitinkevich et al. 2008; Sorbjan 2010). Recently, attempts have been made to relate boundary layer characteristics directly to the wind speed within the boundary layer (in a dimensional or dimensionless form) (see, e.g., Sun et al. 2012, 2016; Acevedo et al. 2016; van de Wiel et al. 2012a,b; van Hooijdonk et al. 2015; Vignon et al. 2017). However, such a measured wind speed also has the disadvantage that it is a result of the boundary layer dynamics itself.

The current study aims to merge the internal and external perspectives by connecting the observed local characteristics to the ambient horizontal pressure gradient (expressed as geostrophic wind speed). Because the latter is derived from the synoptic pressure field, it is not directly influenced by the stability and can be considered to be an external parameter. We construct a climatology in order to document the boundary layer response (fluxes and profiles) over a wide range of geostrophic wind speeds for Cabauw, the Netherlands. Using 11 yr of observations (2005–15), nights are grouped according to their average geostrophic wind speed. Ensemble averages are constructed of these groups. Using such an approach, the mean dynamical response to varying geostrophic wind speed is obtained, while nonsystematic variability is averaged out. To the best of our knowledge, this is the first time that such a classification of boundary layer dynamics in terms of the geostrophic wind speed is presented. Note that our philosophy is inspired by a preliminary study of Bosveld and Beyrich (2004), who classified the NBL at Cabauw with the 200-m wind speed as a proxy for the geostrophic wind speed. Recently, geostrophic wind data from Cabauw were used by Donda et al. (2013) in order to relate near-surface stability to external forcing using a simple Ekman model. Our study differs from Donda et al. (2013) by its focus on climatological interpretation rather than on conceptual modeling.

A detailed climatology will be of special interest to the atmospheric modeling community, enabling a comparison of different models with the ensemble behavior of the stable boundary layer at Cabauw under realistic conditions. This allows researchers to assess the overall quality of the model representation (parameterizations) for a large stability range. Over the past 10 yr, considerable progress has been reported by the GEWEX Atmospheric Boundary Layer Study (GABLS) consortium (see Holtslag et al. 2013). This international collaboration aims to improve parameterizations of the NBL in weather and climate models (see, e.g., Sandu et al. 2013).

Efforts have been effective in pinpointing model capabilities and deficiencies in predicting NBL characteristics such as the near-surface temperature profile, the boundary layer height, and the magnitude of the low-level jet. The intercomparison cases GABLS1 and GABLS2 have been limited to prescribing one constant geostrophic wind speed of $8 \, \mathrm{m \, s}^{-1}$ (Cuxart et al. 2006) and $9.5 \, \mathrm{m \, s}^{-1}$ (Svensson et al. 2011), respectively. Likewise, GABLS3 and GABLS4 prescribe time-dependent geostrophic winds of approximately $8 \, \mathrm{m \, s}^{-1}$ (Bosveld et al. 2014) and 5–$6 \, \mathrm{m \, s}^{-1}$ in magnitude near the surface (E. Bazile 2016, personal communication), respectively. However, to our knowledge a systematic evaluation of model performance for a broad range of geostrophic wind speeds with respect to the observed NBL has yet to be addressed in the literature.

Apart from parameterization issues related to NWP, this climatology could be of interest to idealized model studies using, for example, LESs. Turbulence is largely resolved and different LES model studies show consistent results on average for weakly stable conditions with strong geostrophic winds (see, e.g., Derbyshire 1999; Beare et al. 2006). However, for increasing stability, LESs remain a challenge because of the decrease in the turbulent length scale, and the results become dominated by the subgrid scheme (Beare et al. 2006; Basu and Porté-Agel 2006). In these conditions, flow laminarization may occur as shown, for example, by Jiménez and Cuxart (2005).

It is well known that cases with very weak turbulence commonly occur in reality under strongly stratified conditions (Poulos et al. 2002; Mahrt and Vickers 2006; Mahrt 2011). Here, we will show that those conditions prevail when the geostrophic wind speeds/pressure gradients are small (as expected). With weak winds, the turbulent heat fluxes may become negligibly small. At the same time, the near-surface thermal gradient remains finite and excessive cooling does not seem to occur. This implies that other thermodynamic processes like radiative and soil heat transport become dominant. Hence, we will argue that for realistic modeling of observed climatologies these processes are equally important as turbulent heat transport.

In section 2a, a short description of the measurements at Cabauw and the determination of the near-surface pressure gradient (geostrophic wind speed) is given. The observational analysis procedure is described in section 3, followed by the main results in section 4 and discussion in section 5. Section 6 describes our conclusions.

2. Observations

a. In situ Cabauw

The observations used in this study were obtained at Cabauw, the Netherlands (51.971°N, 4.927°E). The surrounding terrain has relatively flat topography with surface elevations of less than 1 m, and the area is mainly covered by grassland. A detailed description of the site may be found in van Ulden and Wieringa (1996). Main tower measurements of the wind speed (cup anemometers) and the temperature (KNMI Pt500-elements) are obtained at 40, 80, 140, and 200 m, and stored at 10-min intervals. Wind speed is measured at two booms for each level at approximately 10 m from the center of the tower. The temperature and wind speed measurements at 10 and 20 m are measured at an auxiliary mast. To minimize the effects of flow obstruction, instruments from the undisturbed wind sections are selected per 10-min interval. Additionally, the temperature is measured at 1.5 m. The near-surface fluxes are calculated by applying the eddy-covariance technique to measurements from a 5-m flux tower. All components of the net radiation are determined individually at a height of 1.5 m above the surface. Detailed information on the tower measurements, tower positions, and instrumentation may be found in Bosveld (2016).

b. Near-surface pressure gradient

The near-surface pressure gradient at Cabauw is derived from pressure observations of the national meteorological network in the Netherlands at 10-min intervals up to a distance of 200 km from Cabauw. This pressure gradient can be calculated with high accuracy as a result of the high-quality pressure observations taken over the Netherlands and the North Sea, and the relatively flat topography of the Netherlands. First, the pressure observations are corrected for height differences; that is, they are transformed to mean sea level values. Second, a two-dimensional quadratic polynomial is fitted to the observations to obtain the pressure field over the Netherlands. From the curved pressure field the near-surface pressure gradient is calculated by taking the gradient at Cabauw. For interpretation purposes, the magnitude of the near-surface pressure gradient is written as the geostrophic wind speed,

$$U_{\text{geo}} = \frac{1}{\rho_0 f} |\nabla P|, \tag{1}$$

in which ρ_0 is a reference air density and $f = 2\Omega \sin\phi$ is the Coriolis frequency calculated, with Ω being the angular velocity of the earth and ϕ the latitude of Cabauw. An accuracy of 0.1 hPa in the pressure observations is

assumed, resulting in standard deviations of 0.28 and 0.26 m s^{-1} in the latitudinal and longitudinal components of the geostrophic wind, respectively. Note that this does not imply that the actual wind above the boundary layer is in geostrophic balance. A more detailed description may be found in Bosveld et al. (2014).

3. Observational analysis

Following Baas et al. (2012) and van Hooijdonk et al. (2015), we calculate averaged quantities from multi-night ensembles. It is expected that by such a procedure the general dynamical behavior of the stable boundary layer will be clarified because the variability of individual nights is largely averaged out. This averaged-out variability may include, for example, wave activity, meandering of the flow, and local circulation patterns.

a. Selection and classification procedure

The observations are partitioned into 24 h starting at 0900 UTC, such that each period contains one full night. Periods during which one or more gaps exceeding 50 min are present are removed from the dataset. Using a similar approach to van Hooijdonk et al. (2015), the time is subsequently shifted to set $t = 0$ h when the net radiation Q_n becomes negative for more than 1 h. The scope of this study is limited to studying the dynamics as a function of varying geostrophic wind speed. Since it is known that clouds may crucially affect the boundary layer dynamics, only clear-sky nights are considered (see, e.g., Bosveld and Beyrich 2004; Donda et al. 2013). A clear-sky filter selects nights based on an averaged net radiation $\overline{Q_n} \leq -30$ W m^{-2} and standard deviation $\sigma(Q_n) \leq 0.5|\overline{Q_n}|$ between $t = 0$ and 8 h. The aforementioned selection results in a subset of 1969 nights (~50% of the total of 4016). A more stringent criterion of the standard deviation $\sigma(Q_n) = 15$ W m^{-2} was also tested and resulted in a smaller number of selected nights (1303). This did not significantly affect the results, however; variability was slightly increased for geostrophic wind speeds $U_{\text{geo}} \gtrsim 12$ m s^{-1}.

Nights are classified into 1 m s^{-1} geostrophic wind speed bins according to the mean geostrophic wind speed between times $t = -4$ and 8 h. Our analysis is limited to $t < 8$ h to avoid the effects of the morning transition for short nights during the summer. Additionally, only nights during which the standard deviation of U_{geo} is ≤ 1.5 m s^{-1} are considered. Nights with geostrophic wind speeds >16 m s^{-1} are removed because of the small number of nights within these classes ($N < 20$). The resulting total number of nights after these additional steps is 1165. Table 1 gives an overview of the selection procedure, and Table 2 lists the different

TABLE 1. Overview of the selection procedure and criteria for the nights.

Selection step	Criterion	No. of nights
1 Jan 2005–31 Dec 2015	—	4016
Missing-data filter	Gaps ≥ 50 min in U_{geo}, θ, or Q_n	4002
Clear-sky filter	$\overline{Q_n} \leq -30$ W m^{-2} and $\sigma(Q_n) \leq 0.5|\overline{Q_n}|$ between $t = 0$ and 8 h	1969
Filter excluding nights with large variability in the geostrophic wind speed	$\sigma(U_{geo}) \leq 1.5$ m s^{-1}	1228
Filter removing bins with too few nights	Bin count ≥ 20	1165

classes and the number of nights N within each class. More information about the seasonal distribution of the selected nights may be found in the appendix.

b. Ensemble geostrophic wind forcing

As mentioned in the previous section, nights are discarded if the standard deviation of the geostrophic wind speed is larger than 1.5 m s^{-1}. This criterion is used to limit the variability in the ensemble-averaged geostrophic wind speed. The value of this criterion results from a trade-off between variability in the ensemble averaged value of the geostrophic wind speed and the number of nights. Applying a more-strict criterion (e.g., 1 m s^{-1}) leads to a reduction of data by approximately 25%, which in turn leads to a reduction in the statistics and more scatter in the turbulent fluxes.

The temporal evolution of the ensemble-averaged geostrophic wind speed is shown in Fig. 1. The ensemble averaged value for each class shows variation around the bin center values on the order of 0.5 m s^{-1}. The two lowest classes of geostrophic wind speed show a systematic temporal variation in which a minimum value is reached around $t = 2$ h. This diurnal cycle in the pressure gradient likely occurs as a result of the land–sea temperature contrast in the Netherlands (Tijm et al. 1999; He et al. 2013). This is most apparent under conditions of weak large-scale pressure gradients. However, under these conditions the dependence of the NBL on the geostrophic wind speed is weakest and the effect on our classification is probably small (cf. Fig. 7a).

TABLE 2. Overview of the classes and number of nights within each class.

Class (m s^{-1})	N	Class (m s^{-1})	N
[1; 2)	40	[9; 10)	103
[2; 3)	67	[10; 11)	83
[3; 4)	83	[11; 12)	56
[4; 5)	112	[12; 13)	54
[5; 6)	109	[13; 14)	50
[6; 7)	115	[14; 15)	33
[7; 8)	117	[15; 16)	28
[8; 9)	115		

4. Results

In this section, ensemble-averaged quantities such as radiative and turbulent fluxes, along with vertical profiles, are analyzed. The results show that the ensemble averages are remarkably well organized in terms of their corresponding geostrophic forcing. For all classes an approximately stationary state of most quantities is reached at $t = 2$ h.

a. Radiation

Figures 2a,b show the temporal evolution of the net shortwave radiation S_n (down- minus upwelling shortwave radiation) and the total net radiation Q_n for the different geostrophic wind speed classes. For all classes, it is observed that on average the total net radiation becomes negative approximately 1.5 h before the incoming shortwave radiation becomes zero, indicating that radiative cooling of the surface starts before sunset. Furthermore, the net shortwave radiation before sunset appears to be inversely correlated with the geostrophic wind speed, which is probably caused by the relatively small number of winter cases having low geostrophic wind speeds (cf. Fig. A1).

Prior to $t = 0$ h there appears to be no systematic trend between the net radiation (see Fig. 2b) and the
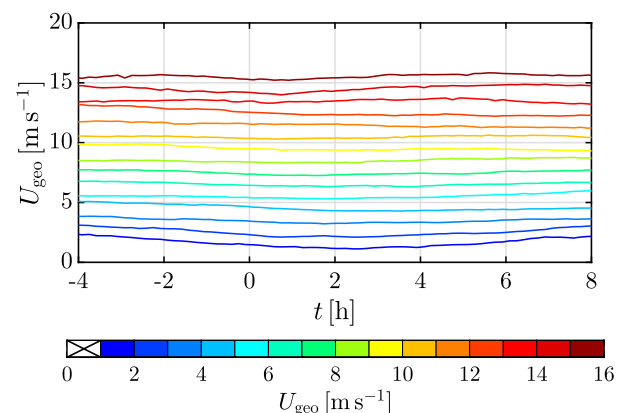

FIG. 1. Temporal evolution of the ensemble-averaged geostrophic wind speed. The color coding indicates the classes of the geostrophic wind speed and is kept the same in all subsequent figures concerning the different classes.
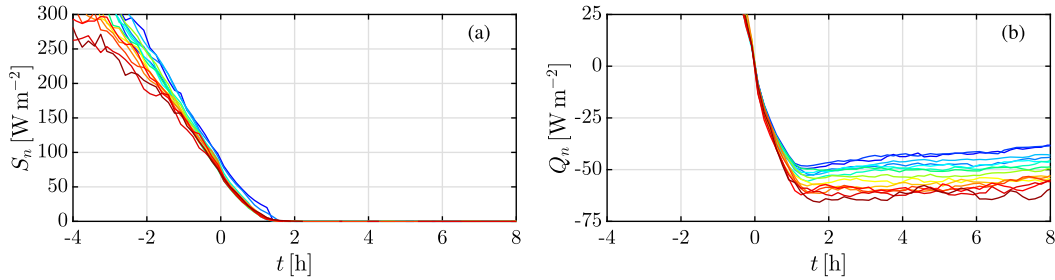
FIG. 2. Temporal evolution of (a) the net shortwave radiation and (b) the net radiation for all geostrophic wind speed classes. The color coding is given in Fig. 1.

magnitude of the geostrophic wind. However, after approximately $t = 2$ h a systematic trend is observed in which the absolute value of the net radiation decreases for decreasing geostrophic wind speed. The net radiation levels off to a value of approximately -60 W m^{-2} for the highest wind class, $U_{geo} \in [15; 16]$ m s^{-1}, while the value for the lowest class reaches approximately -50 W m^{-2} between 1 and 2 h, and afterward increases to -40 W m^{-2} at 8 h. These observations are consistent with the expected trend in surface temperature. The stronger thermal gradient in weak wind conditions helps explain the lower net radiative cooling under those conditions; the relatively low surface temperature and outgoing longwave radiation result in a smaller magnitude of net radiative cooling relative to the stronger wind case with relatively high surface temperatures. It is not, however, excluded that the differences among different classes of geostrophic wind speed are influenced by the seasonal distribution of the selected nights (see Fig. A1). For example, net radiative loss will be lower in summer as a result of the higher moisture content of the lower atmosphere. Further analysis reveals that the difference between summer and winter may amount up to 15 W m^{-2} (not shown).

b. Turbulent fluxes

The turbulent stress and the turbulent sensible heat flux are shown in Figs. 3a and 3b, respectively. Both

figures show a clear organization of the data according to classes of constant geostrophic wind speed after $t = 0$ h. For geostrophic wind speeds $U_{geo} \leq 4$ m s^{-1}, both the average turbulent stress and the average turbulent sensible heat flux tend to become negligibly small, suggesting that cases in which turbulent mixing is virtually absent are quite common at Cabauw. This has important implications for the numerical modeling of the stable boundary layer. In particular LESs might have difficulty in resolving those small flux cases (see Beare et al. 2006; Holtslag et al. 2013).

The turbulent stress decreases in the late afternoon as a result of the transition toward the stable boundary layer, and tends to level off for $t \geq 2$ h. For the highest wind classes, the stress is reduced to approximately 40% of its pretransition value, while for the lowest wind speed classes it is reduced to approximately 2%–3% of its initial value. Contrary to the findings of van Hooijdonk et al. (2015) and Donda et al. (2015), no increase in turbulent stress during the night is found (for the very stable cases). They attributed this increase to a force imbalance between the horizontal pressure force and frictional forces after an initial decrease of turbulent friction (see, e.g., Donda et al. 2015).

A similar pattern of behavior is observed for the turbulent heat flux (Fig. 3b). During the afternoon the heat flux decreases from positive values (i.e., directed from the surface to the atmosphere) and becomes negative
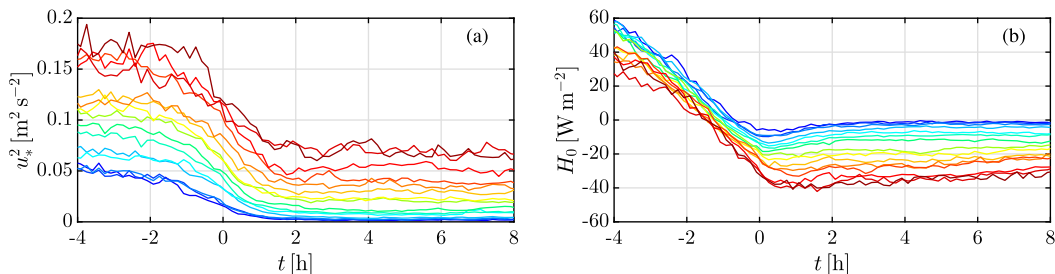

FIG. 3. As in Fig. 2, but for (a) the turbulent stress and (b) the turbulent heat flux.
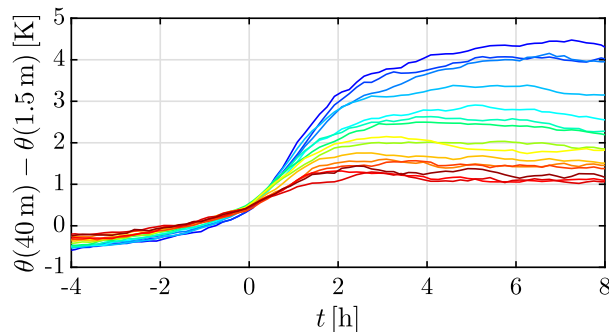
FIG. 4. Temporal evolution of the thermal gradient between 40 and 1.5 m. The color coding is given in Fig. 1.

between $t = -1.5$ and -0.5 h. This indicates that cooling of the surface layer occurs *before* the change of sign of the net radiation (see section 4c and the references therein). A slight minimum in the heat flux is present between $t = 0$ and 1 h as the NBL passes a stage of intermediate stability from neutral to more stable later in the night. For $t \gtrsim 2$ h, the turbulent heat flux also tends to an approximately constant value. This quasi-steady value is dependent on the magnitude of the geostrophic wind and is robust when conditioned on different seasons.

c. Thermal gradient

In Fig. 4 the time-dependent gradient of the potential temperature is shown for the different classes. This thermal gradient is defined as the difference in potential temperature between 40 and 1.5 m. The 1.5-m level is the lowest level present in the 11-yr dataset considered. A temperature probe at 10 cm above the surface has been in operation since August 2013, but its dataset is too limited to be used for the current ensemble analysis. Recent results by van de Wiel et al. (2017) employing the limited dataset with the 10-cm probe indicate that the additional difference between 1.5 and 0.1 m may be up to 5 K for low wind speeds.

The thermal gradient prior to the onset of the NBL, $t \leq -1$ h, shows weak dependence on the geostrophic wind, although a tendency toward more neutral stratification is observed for high wind conditions, as expected. Note that, during the daytime, turbulent transport by convection causes the gradient magnitude to remain small (<0.7 K). Similar to the turbulent heat flux, the gradient becomes positive approximately 1 h before the net radiation is zero (cf. Figs. 2 and 3). This change of sign is followed by a rapid increase in the gradient up to approximately $t = 2$ h.

As shown in Figs. 2–4, the onset of the stable boundary layer (time at which the turbulent heat flux becomes negative) is not synchronous with either zero shortwave

radiation or zero net radiation. This moment is likely dictated by the latent heat flux associated with evapotranspiration. In the afternoon, as the air flows over a relatively wet surface, the continuous demand for energy for evaporation may result in negative sensible heat fluxes in otherwise convective conditions (Moene and van Dam 2014, chapter 7). Unfortunately, no systematic analysis on this interesting aspect could be performed because of observational limitations. For example, the eddy-covariance measurements tend to underestimate the latent heat flux, especially for increasing stability. Furthermore, at low wind speeds dew formation on the instruments results in a large amount of missing values. For a detailed analysis of the latent heat flux in relation to the closure of the surface energy balance, we refer to De Roode et al. (2010).

d. Wind and temperature profiles

Figures 5a–f show the ensemble profiles of the measured wind speed and the relative potential temperature θ_{relative} for three classes of geostrophic wind speeds at times $t = -3$, 0, 3, and 6 h. The latter is defined by subtracting the 200-m potential temperature at $t = 0$ h from all observations, i.e., $\theta_{\text{relative}} = \theta(z) - \theta_0(200 \text{ m})$. For all three classes, the wind profiles at 3 and 6 h are nearly identical, which indicates that they have reached a quasi-stationary state. This is most prominently observed for the highest geostrophic wind speed class.

In correspondence with van de Wiel et al. (2012a), a "crossing level" (i.e., the height at which the wind speed stays relatively constant) can be identified for the intermediate and highest class. However, this level is not equal for both cases; it is between 40 and 50 m for the [6; 7] class and between 70 and 80 m for the [14; 15] m s^{-1} class. Between $t = 0$ and 3 h the wind accelerates above the crossing level, while it decreases below the crossing level as a result of the increased stress divergence with height resulting from stability (Baas et al. 2012). No crossing level is observed for the lowest geostrophic wind speed class [1; 2] m s^{-1}. During the afternoon ($t = -3$ h) the magnitude of the wind speed along the entire tower height is approximately twice the value of the geostrophic wind speed during the night. This is probably caused by the geostrophic wind speed being higher during the preceding day (cf. between -4 and -2 h in Fig. 1).

The profiles of potential temperature do not exhibit a stationary state between 3 and 6 h, with cooling along the tower height still occurring, whereas the thermal gradient reaches a roughly stationary value after approximately $t = 3$ h (see Fig. 4). The total surface cooling during the night is significant for all classes and may even
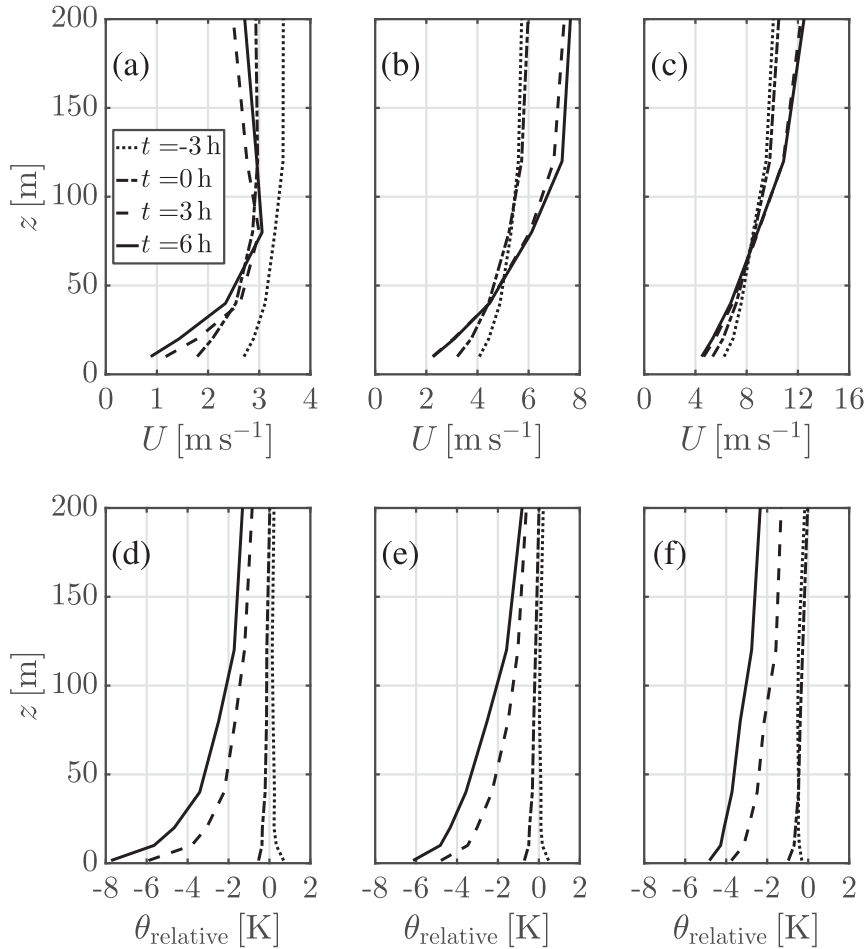
FIG. 5. Vertical profiles of (top) the wind speed and (bottom) the potential temperature for three geostrophic wind speed classes at four different times: (a),(d) [1; 2], (b),(e) [6; 7], and (c),(f) [14; 15] m s^{-1}. The horizontal scale in the wind speed profiles is not equal for each class.

reach up to 5 K for the highest geostrophic wind speed shown. By contrast, the relative differences between heights remain small for this geostrophic wind speed. For the lowest geostrophic wind speed class shown, the resulting profile of potential temperature is strongly convex, exhibiting an exponential profile. Such a profile is an indication that the surface layer is decoupled from higher levels (André and Mahrt 1982; Estournel and Guedalia 1985).

e. Steady-state fluxes

After the initial transition period, the averaged turbulent fluxes do not vary significantly relative to those during the time $t \leq 2$ h (see Fig. 3). Therefore, we will refer to the period between $t = 3$ and 6 h as the "quasi-steady state" of the stable boundary layer. Note that apart from the turbulent fluxes, Fig. 2 indicates that

the magnitude of the net radiation itself is decreasing during the night in response to the changing vertical profiles of temperature (see Figs. 5d–f) and moisture (not shown). The quasi-steady fluxes and their features reported in this section are found to be robust when limiting the data to single seasons. However, a detailed analysis of the seasonal effects is beyond the scope of this work.

Figure 6 shows the quasi-steady values of the turbulent stress per geostrophic wind speed class. The average and median are calculated from the set of all 10-min interval observations in quasi-steady state per class. For increasing geostrophic wind speed, the average and median values of the turbulent stress increase, as expected. In addition, both the standard deviation and the range of values covered (as depicted through the percentile lines) increase with increasing forcing.
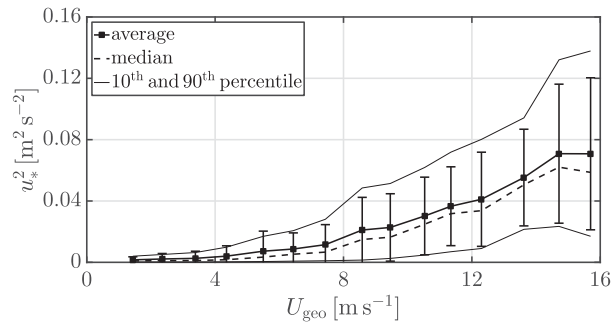
FIG. 6. Turbulent stress vs geostrophic wind forcing in quasi-steady state. The error bars denote 1 standard deviation from the average value, and the thin lines denote the 10th and 90th percentiles of the data.

For geostrophic wind speeds $< 4 \, \text{m s}^{-1}$, the turbulent stress is on the order of $10^{-3} \, \text{m}^2 \, \text{s}^{-2}$, and turbulent activity is negligibly small. Such values may typically be found under extremely weak wind conditions (Mahrt and Vickers 2006; Mahrt 2011). The turbulent stress gradually increases for geostrophic wind speeds larger than $4 \, \text{m s}^{-1}$. In this ensemble analysis no specific threshold value of the geostrophic wind speed is discerned. By contrast, previous studies report threshold values of wind speeds measured along the tower beyond which the turbulent stress sharply increases in magnitude (see, e.g., van Hooijdonk et al. 2015; Sun et al. 2016). The latter would indicate a clear "on–off" mechanism behind the transition between the very stable (VSBL) and weakly stable boundary layer (WSBL). On the other hand, the "quasi laminar" VSBL itself can be populated by sudden interruptions of turbulent bursts. This aspect, known as global intermittency, is in fact expected to occur for intermediate ranges of the geostrophic wind speeds (van de Wiel et al. 2002a; Poulos et al. 2002; Sun et al. 2004; Steeneveld et al. 2006). Recently, Sun et al. (2012) suggested that an intermediate transitional regime exists in which turbulence is intermittent. They hypothesize that this intermittent turbulence is caused by top-down bursting of turbulent flow from above the boundary layer height. Recently, Ansorge and Mellado (2014) demonstrated with direct numerical simulation (DNS) that turbulent patches in an otherwise laminar flow may form in a stably stratified Ekman-type flow without external triggers. The horizontal extent of these patches was found to be dependent on the stratification. Related results were obtained in DNSs of stably stratified open-channel flow by He and Basu (2015). Interestingly, intermittency has also been simulated over realistic terrain using LESs (Zhou and Chow 2014).

Alternating periods of turbulent and laminar parts of the flow may explain this gradual transition from VSBL to WSBL in our averaged quantities.

In Fig. 7, the turbulent friction velocity is given as a function of geostrophic wind speed along with the probability density function (PDF) for the classes $U_{\text{geo}} \in [1; 2)$, $[6; 7)$, $[8; 9)$, and $[14; 15] \, \text{m s}^{-1}$. The probability density function is determined using an automated kernel density estimation (see Botev et al. 2010). The scatter in observed friction velocities is found to increase for increasing geostrophic wind. Both the average and median values follow a systematic trend. The PDFs show that observed friction velocities within classes overlap with those of other classes. For the highest geostrophic wind speed class (in red) the tails extend as far as $u_* \approx 0.05$ and $0.5 \, \text{m s}^{-1}$. The width of the PDF is mainly influenced by the averaging time of the flux sensor of 10 min and by the integral time scale of turbulence (Wyngaard 1973). It is expected that the current averaging time is sufficient to capture most of the significant frequencies in stable conditions (Oncley et al. 1996; Babić et al. 2012). However, it is not excluded that low-frequency contributions to the signal are present, and that an increase in averaging time may reduce the observed spread in friction velocities. Note that this aspect is, however, not trivial. Apart from statistical convergence, the variability in u_* may potentially also increase as a result of the inclusion of additional low-frequency motions. Another possible cause could be short disturbances on the 10-min time scale, such as short changes in local cloud cover.

Additionally, the distribution itself is found to change from nearly Gaussian for the highest geostrophic wind speeds to a strongly skewed distribution approaching a lognormal distribution for the lowest class, $U_{\text{geo}} \in [1; 2) \, \text{m s}^{-1}$. This change in distribution is expected as the friction velocity is nonnegative. For these low geostrophic wind speeds, the width of the distribution is smaller than that for the higher geostrophic wind speeds; that is, the distribution covers only a small range of u_* values. Within this context, van de Wiel et al. (2017) hypothesized that around critical values of the wind speed the "recovery time" of the NBL to perturbations is large, and as such the (normalized) observational scatter peaks at such wind speeds. Although the spread normalized by the average friction velocity shows a clear decreasing trend for $U_{\text{geo}} \gtrsim 8 \, \text{m s}^{-1}$, for low geostrophic wind speeds the spread is rather constant (with a small maximum around $4.5 \, \text{m s}^{-1}$). Therefore, at this stage no conclusions on this interesting aspect can be made.

Interestingly, for intermediate geostrophic wind speeds the distributions appear to be bimodal (green
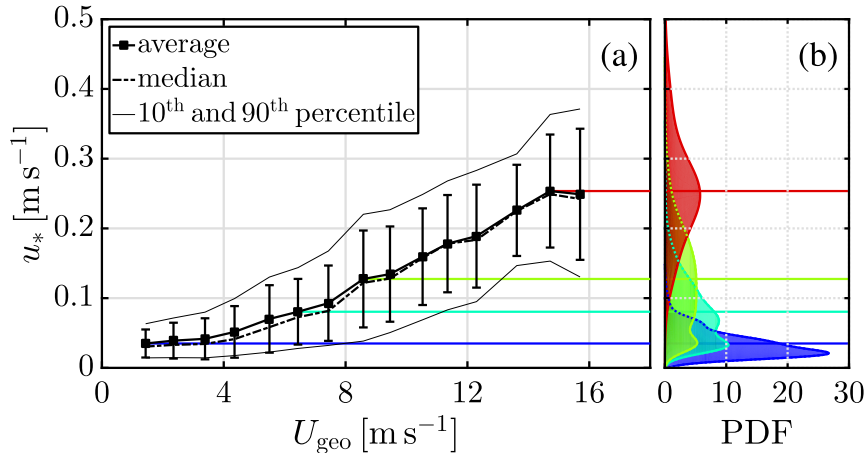
FIG. 7. (a) Turbulent friction velocity vs geostrophic wind forcing in quasi-steady state. The error bars denote 1 standard deviation from the average value, and the thin lines denote the 10th and 90th percentiles of the data. (b) PDF of the observed friction velocities within the time frame 3–6 h for four classes. The colored horizontal lines indicate the position of the average values in the PDF. The color coding is given in Fig. 1.

and light blue PDFs). The first mode (lowest value of u_*) coincides with the peak of the lowest class (dark blue), whereas the second mode resembles the higher geostrophic wind speed classes. Therefore, for the intermediate range of geostrophic wind speeds the boundary layer exhibits characteristics of both the traditional very stable and weakly stable boundary layers. A similar result was recently obtained by Monahan et al. (2015), who found that two separate underlying distributions can be identified in the intermediate local stability range using a hidden-Markov-model analysis. These were found to correlate with geostrophic wind speed and cloud cover (viz., one distribution is more common at low geostrophic wind speed and clear-sky conditions). Likewise, Acevedo et al. (2016) and Dias-Júnior et al. (2017) showed that observations over a wide range of stability fall into two separate distributions associated with the two regimes. As a result, the total distribution is bimodal.

Apart from other physical reasons, a potential explanation for the occurrence of multimodal distributions in the friction velocity is the aforementioned process of global intermittency. During such an intermittent night, the boundary layer would be subject to periods of turbulent bursts in an otherwise quasi-laminar flow. A second explanation is the possibility of local disturbances such as sudden changes in cloud cover, local momentum advection, or small synoptic disturbances. A sensitivity analysis was performed to assess the impact of the net radiation (possible short episodes with clouds) on the observed distribution of friction velocity, but no

relation could be detected in the current results (not shown).

The quasi-steady values of the turbulent heat flux are shown in Fig. 8. In agreement with the turbulent stress the turbulent heat flux shows a gradual transition in magnitude from low to high geostrophic wind speeds. As compared with the heat loss due to net radiation (see Fig. 2b), the supply of heat by turbulent motions is negligible for geostrophic wind speeds of $U_{geo} \leq 4\,\mathrm{m\,s^{-1}}$ (viz. $|H_0| \approx 1$–$4\,\mathrm{W\,m^{-2}}$ vs $|Q_n| = 40\,\mathrm{W\,m^{-2}}$). For these cases, the evolution of the surface temperature is not dramatically different (in order of magnitude) than that of, for example, cases with medium geostrophic wind (cf. Figs. 5d–f). This implies that all thermodynamic transport has to be supplied by the longwave radiation and the surface heat conduction. By contrast, for the highest geostrophic wind speeds the magnitude of the turbulent heat flux is significant at approximately $30\,\mathrm{W\,m^{-2}}$.
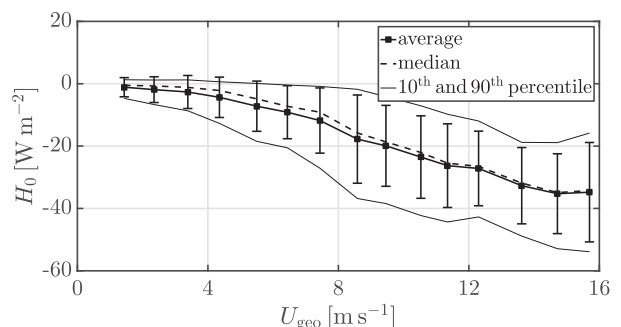

FIG. 8. As in Fig. 6, but for turbulent heat flux.

In Fig. 9 the (quasi steady) thermal gradient between 40 and 1.5 m above the surface is plotted as a function of the geostrophic wind speed. It is noted that this gradient does not reach a quasi-steady state for most classes within the time frame of 3–6 h (also see Fig. 4). However, the change within this period is relatively small (<0.5 K) with the largest change occurring for the lowest four geostrophic wind speed classes. The difference in gradient strength between the lowest and highest geostrophic wind speeds is found to be a factor of 4 (i.e., approximately 1 vs 4 K for both average and median values). In addition, the spread in observed gradients (see percentile lines) is largest for lower geostrophic wind speeds (i.e., 4 vs 2 K).

5. Discussion

a. A critical wind speed?

Previous studies using observations from Cabauw (van Hooijdonk et al. 2015; van de Wiel et al. 2017) indicate the existence of a critical in situ wind speed at which the boundary layer as a whole changes from one regime to the other (in an ensemble sense). Similar studies performed at different measurement sites also predict the existence of a threshold wind speed, for example, Dome C, Antarctica (Vignon et al. 2017); CASES-99 campaign, Kansas (Sun et al. 2012), and Fluxes over Snow Surfaces II (FLOSS II) field campaign, northwest Colorado (Acevedo et al. 2016).

In the current results, however, the change in turbulent fluxes and thermal gradient for different geostrophic wind speeds is found to be gradual. No critical geostrophic wind speed or narrow range of geostrophic wind speeds can be identified at which a clear, sudden, or sharp transition occurs between two distinctive regimes of the nocturnal boundary layer.

A similar result was obtained by Monahan et al. (2015), who found two regimes corresponding to a weak turbulence and high turbulence state. The weak turbulence regime was found to correlate with clear skies and low geostrophic wind speeds, while the other regime correlated with cloudy conditions and large geostrophic wind speeds. However, they did not find a clear transition between regimes, and both regimes were found to overlap for a range of geostrophic wind speeds and cloud cover, in agreement with the present study.

In practice, the geostrophic wind speed is not the only external forcing of the system. Atmospheric influences of the NBL include atmospheric moisture, advection of momentum and temperature (which may depend on the season or wind direction), and variable cloud cover. External parameters linked to the surface
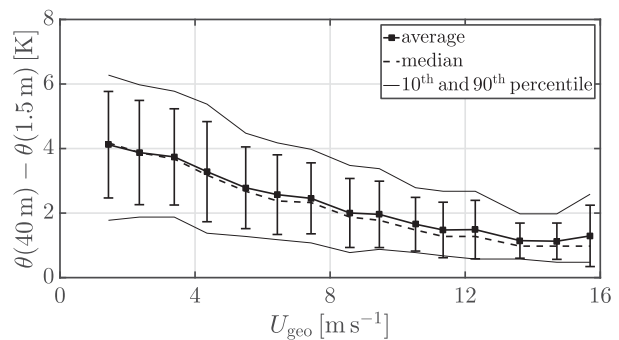

FIG. 9. As in Fig. 6, but for the thermal gradient between 40 and 1.5 m.

are, for example, local topography and directional dependence of the roughness or the availability of soil moisture, which changes both the heat conductance and the heat capacity of the soil. These parameters can crucially influence the dynamics and regime of the NBL through the production of turbulent mixing, as well as the surface energy budget. Furthermore, a (small) seasonal dependence on the longwave radiative loss directly affects the energy demand.

The influences of these other external parameters on the regime transition are not represented in the geostrophic wind speed. However, they are implicitly observed in the near-surface wind speed, which, as an internal parameter, depends on them via the internal dynamical behavior of the NBL.

If the geostrophic wind speed is the only independent variable (all other parameters are kept fixed), a unique "sharp" transition is expected to occur at a critical value of this wind speed (disregarding aspects of global intermittency). Indeed, such behavior has been shown by both simplified models (McNider et al. 1995; van de Wiel et al. 2002b; Shi et al. 2005; Costa et al. 2011) and well-controlled numerical studies (Nieuwstadt 2005; Donda et al. 2015). On the contrary, if (natural) variability of the other external parameters is included (via Monte Carlo analysis) in the simulations, a smoother pattern of behavior would have also occurred. Also, simulations using a more realistic model configuration, for example, with the clear-air radiative transport, presented in McNider et al. (2012), support a more gradual response of the NBL to changing geostrophic wind as in conceptual models.

Furthermore, identification of a critical transition geostrophic wind speed is possibly partly obscured by an intermediate state in which the boundary layer is intermittent. Both fluxes and the local wind speed will vary on a much shorter time scale (i.e., temporarily occupying turbulent and nonturbulent states) than the variation

in the forcings such that short-term correspondence is lost (A. H. Monahan 2017, personal communication). Likewise, during intermittent events, wind speeds near the surface (e.g., the 40-m wind speed) will likely react in coherence with turbulence characteristics such as the friction velocity, thereby keeping the relation among these attributes unique.

In summary, whereas internal parameters such as the 40-m wind speed effectively probe the internal state of the system, the geostrophic wind speed does not have knowledge of the realistic variability of other forcings and changing local parameters.

b. Model implications

The current results show that for low geostrophic wind speeds ($U_{geo} \leq 4 \, \text{m s}^{-1}$) the ensemble-averaged turbulent mixing of both momentum and heat is negligibly small after transition to a quasi-steady stable boundary layer (see Figs. 6 and 8). For these geostrophic wind speeds, the observed sensible heat fluxes are found to be on the order of $H_0 = 1–4 \, \text{W m}^{-2}$. However, the radiative loss of energy at the surface remains substantial at approximately $|Q_n| = 40 \, \text{W m}^{-2}$ (see Fig. 2b). At the same time this does not lead to excessive cooling, which implies that other processes, such as radiative heat transfer and heat conduction through soil and vegetation, take over the thermodynamic transport. Large, rapid surface cooling may occur, when the soil heat conduction is inhibited by, for example, snow cover, until natural radiative limits are reached (see Whiteman et al. 2004). This is an important insight with significant implications for advanced models that resolve turbulence such as LESs and DNSs. To accurately represent boundary layers, models need to take into account the heat exchange with an underlying surface (soil and/or vegetation), radiative transfer, and heat transport associated with evapotranspiration. In fact, this requires that a similar degree of complexity be included in the implementation of different processes; for example, soil interaction cannot just be modeled as simple temperature or flux boundary conditions (Steeneveld et al. 2006).

6. Conclusions

In the current work, the clear-sky nocturnal boundary layer at Cabauw is investigated using the geostrophic wind speed as a classification parameter. Eleven years' worth of observational data are selected on clear nights and grouped according to the average geostrophic wind speed within a night. Subsequently, ensemble-average time series of, for example, turbulent fluxes and profiles are calculated. This procedure reduces the observational variability often found within single nights, and emphasizes the underlying generic dynamics. As such, a benchmark set for numerical models is obtained.

We found that the geostrophic wind is an important parameter describing the evolution of the nocturnal boundary layer and results in a gradual ordering of the diagnosed variables. For Cabauw, the transition from the weakly stable to the very stable boundary layer is not abrupt for decreasing geostrophic forcing, but gradual in nature for ensemble-averaged diagnostic variables. This is in contrast to the sharp transition found when turbulent fluxes are related to the (instantaneous) tower wind speed, and as predicted in conceptual models. For intermediate geostrophic wind speeds, the observed distributions of the turbulent friction velocity appear to be bimodal, whereas in both the weakly and very stable limit the distributions are unimodal.

As the geostrophic wind speed is not the only external parameter, the regime separation is obscured by, for example, soil and atmospheric moisture, advection, and variable cloud cover. Apart from these parameters, we suggest that this behavior can also potentially be explained by the occurrence of globally intermittent turbulence in which sudden moments of turbulent bursts appear in a quasi-laminar boundary layer. Further research is needed to investigate this hypothesis. High-resolution, turbulence-resolving simulations, such as LESs and DNSs, are expected to provide valuable insights with respect to the regime transition and global intermittency. However, any realistic simulation under weak turbulent conditions for the boundary layer evolution at Cabauw would have to include realistic heat transport by radiation, soil, and evapotranspiration.

Finally, more research is needed into the applicability of the current results to other climates. Van de Wiel et al. (2017) showed that the near-surface thermal gradient under weak wind conditions critically depends on the coupling strength of the land to the atmosphere. The current results also indicate that the onset of the NBL depends on evapotranspiration in the afternoon. It would therefore be interesting to apply the current analysis to other regions provided that both long-term local measurements and an accurate estimate of the geostrophic wind (either from pressure observations or model reanalysis) are available.
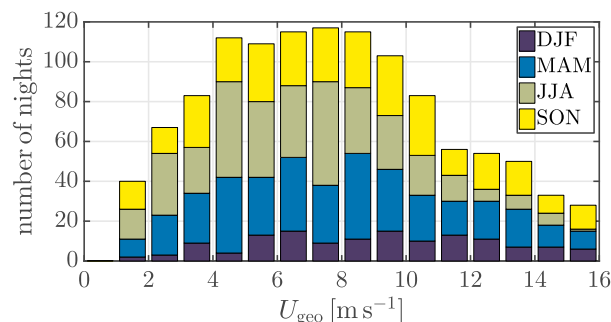
FIG. A1. Seasonal distribution of all selected nights per geostrophic wind speed class.

APPENDIX

Seasonal Distribution

In section 3a, the selection and classification procedure is outlined along with the total number of selected nights per class. Here, an overview of the seasonal distribution of these selected nights is given in Fig. A1. The relative contribution of the (more cloudy) winter season (December–February) is smallest for all classes as a result of the clear-sky and geostrophic wind speed filters.

REFERENCES

Acevedo, O. C., L. Mahrt, F. S. Puhales, F. D. Costa, L. E. Medeiros, and G. A. Degrazia, 2016: Contrasting structures between the decoupled and coupled states of the stable boundary layer. *Quart. J. Roy. Meteor. Soc.*, **142**, 693–702, doi:10.1002/qj.2693.

André, J. C., and L. Mahrt, 1982: The nocturnal surface inversion and influence of clear-air radiative cooling. *J. Atmos. Sci.*, **39**, 864–878, doi:10.1175/1520-0469(1982)039<0864:TNSIAI>2.0.CO;2.

Ansorge, C., and J. P. Mellado, 2014: Global intermittency and collapsing turbulence in the stratified planetary boundary layer. *Bound.-Layer Meteor.*, **153**, 89–116, doi:10.1007/s10546-014-9941-3.

Baas, P., B. J. H. van de Wiel, L. van den Brink, and A. Holtslag, 2012: Composite hodographs and inertial oscillations in the nocturnal boundary layer. *Quart. J. Roy. Meteor. Soc.*, **138**, 528–535, doi:10.1002/qj.941.

Babić, K., Z. Bencetić, and Ž. Večenaj, 2012: Determining a turbulence averaging time scale by Fourier analysis for the nocturnal boundary layer. *Geofizika*, **29**, 35–51.

Basu, S., and F. Porté-Agel, 2006: Large-eddy simulation of stably stratified atmospheric boundary layer turbulence: A scale-dependent dynamic modeling approach. *J. Atmos. Sci.*, **63**, 2074–2091, doi:10.1175/JAS3734.1.

Beare, R. J., and Coauthors, 2006: An intercomparison of large-eddy simulations of the stable boundary layer. *Bound.-Layer Meteor.*, **118**, 247–272, doi:10.1007/s10546-004-2820-6.

Bosveld, F. C., 2016: Cabauw In-situ Observational Program 2000—Now: Instruments, calibrations and set-up. KNMI Tech. Rep., 77 pp., http://projects.knmi.nl/cabauw/insitu/observations/documentation/Cabauw_TR/Cabauw_TR.pdf.

——, and F. Beyrich, 2004: Classifying observations of stable boundary layers for model validation. *16th Symp. on Boundary Layers and Turbulence*, Portland, ME, Amer. Meteor. Soc., P4.13, https://ams.confex.com/ams/pdfpapers/78641.pdf.

——, P. Baas, E. van Meijgaard, E. I. F. de Bruijn, G. J. Steeneveld, and A. A. M. Holtslag, 2014: The third GABLS intercomparison case for evaluation studies of boundary-layer models. Part A: Case selection and set-up. *Bound.-Layer Meteor.*, **152**, 133–156, doi:10.1007/s10546-014-9917-3.

Botev, Z. I., J. F. Grotowski, and D. P. Kroese, 2010: Kernel density estimation via diffusion. *Ann. Stat.*, **38**, 2916–2957, doi:10.1214/10-AOS799.

Costa, F. D., O. C. Acevedo, J. C. M. Mombach, and G. A. Degrazia, 2011: A simplified model for intermittent turbulence in the nocturnal boundary layer. *J. Atmos. Sci.*, **68**, 1714–1729, doi:10.1175/2011JAS3655.1.

Cuxart, J., and Coauthors, 2006: Single-column model intercomparison for a stably stratified atmospheric boundary layer. *Bound.-Layer Meteor.*, **118**, 273–303, doi:10.1007/s10546-005-3780-1.

Derbyshire, S. H., 1999: Stable boundary-layer modelling: Established approaches and beyond. *Bound.-Layer Meteor.*, **90**, 423–446, doi:10.1023/A:1001749007836.

De Roode, S. R., F. C. Bosveld, and P. S. Kroon, 2010: Dew formation, eddy-correlation latent heat fluxes, and the surface energy imbalance at Cabauw during stable conditions. *Bound.-Layer Meteor.*, **135**, 369–383, doi:10.1007/s10546-010-9476-1.

Dias-Júnior, C. Q., L. D. Sá, E. P. Marques Filho, R. A. Santana, M. Mauder, and A. O. Manzi, 2017: Turbulence regimes in the stable boundary layer above and within the Amazon forest. *Agric. For. Meteor.*, **233**, 122–132, doi:10.1016/j.agrformet.2016.11.001.

Donda, J. M. M., B. J. H. van de Wiel, F. C. Bosveld, F. Beyrich, G. J. F. van Heijst, and H. J. H. Clercx, 2013: Predicting nocturnal wind and temperature profiles based on external forcing parameters. *Bound.-Layer Meteor.*, **146**, 103–117, doi:10.1007/s10546-012-9755-0.

——, I. G. S. van Hooijdonk, A. F. Moene, H. J. J. Jonker, G. J. F. van Heijst, H. J. H. Clercx, and B. J. H. van de Wiel, 2015: Collapse of turbulence in stably stratified channel flow: A transient phenomenon. *Quart. J. Roy. Meteor. Soc.*, **141**, 2137–2147, doi:10.1002/qj.2511.

Estournel, C., and D. Guedalia, 1985: Influence of geostrophic wind on atmospheric nocturnal cooling. *J. Atmos. Sci.*, **42**, 2695–2698, doi:10.1175/1520-0469(1985)042<2695:IOGWOA>2.0.CO;2.

Grachev, A. A., C. W. Fairall, P. O. G. Persson, E. L Andreas, and P. S. Guest, 2005: Stable boundary-layer scaling regimes: The SHEBA data. *Bound.-Layer Meteor.*, **116**, 201–235, doi:10.1007/s10546-004-2729-0.

He, P., and S. Basu, 2015: Direct numerical simulation of intermittent turbulence under stably stratified conditions. *Nonlinear Processes Geophys.*, **22**, 447–471, doi:10.5194/npg-22-447-2015.

He, Y., A. H. Monahan, and N. A. McFarlane, 2013: Diurnal variations of land surface wind speed probability distributions under clear-sky and low-cloud conditions. *Geophys. Res. Lett.*, **40**, 3308–3314, doi:10.1002/grl.50575.

Holtslag, A. A. M., and Coauthors, 2013: Stable atmospheric boundary layers and diurnal cycles: Challenges for weather and climate models. *Bull. Amer. Meteor. Soc.*, **94**, 1691–1706, doi:10.1175/BAMS-D-11-00187.1.

Jiménez, M. A., and J. Cuxart, 2005: Large-eddy simulations of the stable boundary layer using the standard Kolmogorov theory:

Range of applicability. *Bound.-Layer Meteor.*, **115**, 241–261, doi:10.1007/s10546-004-3470-4.

Mahrt, L., 1998: Nocturnal boundary-layer regimes. *Bound.-Layer Meteor.*, **88**, 255–278, doi:10.1023/A:1001171313493.

——, 2011: The near-calm stable boundary layer. *Bound.-Layer Meteor.*, **140**, 343–360, doi:10.1007/s10546-011-9616-2.

——, and D. Vickers, 2006: Extremely weak mixing in stable conditions. *Bound.-Layer Meteor.*, **119**, 19–39, doi:10.1007/s10546-005-9017-5.

Mauritsen, T., and G. Svensson, 2007: Observations of stably stratified shear-driven atmospheric turbulence at low and high Richardson numbers. *J. Atmos. Sci.*, **64**, 645–655, doi:10.1175/JAS3856.1.

McNider, R. T., D. E. England, M. J. Friedman, and X. Shi, 1995: Predictability of the stable atmospheric boundary layer. *J. Atmos. Sci.*, **52**, 1602–1614, doi:10.1175/1520-0469(1995)052<1602:POTSAB>2.0.CO;2.

——, and Coauthors, 2012: Response and sensitivity of the nocturnal boundary layer over land to added longwave radiative forcing. *J. Geophys. Res.*, **117**, D14106, doi:10.1029/2012JD017578.

Moene, A. F., and J. van Dam, 2014: *Transport in the Atmosphere–Vegetation–Soil Continuum.* Cambridge University Press, 446 pp.

Monahan, A. H., T. Rees, Y. He, and N. McFarlane, 2015: Multiple regimes of wind, stratification, and turbulence in the stable boundary layer. *J. Atmos. Sci.*, **72**, 3178–3198, doi:10.1175/JAS-D-14-0311.1.

Nieuwstadt, F. T. M., 2005: Direct numerical simulation of stable channel flow at large stability. *Bound.-Layer Meteor.*, **116**, 277–299, doi:10.1007/s10546-004-2818-0.

Oncley, S. P., C. A. Friehe, J. C. Larue, J. A. Businger, E. C. Itsweire, and S. S. Chang, 1996: Surface-layer fluxes, profiles, and turbulence measurements over uniform terrain under near-neutral conditions. *J. Atmos. Sci.*, **53**, 1029–1044, doi:10.1175/1520-0469(1996)053<1029:SLFPAT>2.0.CO;2.

Poulos, G. S., and Coauthors, 2002: CASES-99: A comprehensive investigation of the stable nocturnal boundary layer. *Bull. Amer. Meteor. Soc.*, **83**, 555–581, doi:10.1175/1520-0477(2002)083<0555:CACIOT>2.3.CO;2.

Sandu, I., A. Beljaars, P. Bechtold, T. Mauritsen, and G. Balsamo, 2013: Why is it so difficult to represent stably stratified conditions in numerical weather prediction (NWP) models? *J. Adv. Model. Earth Syst.*, **5**, 117–133, doi:10.1002/jame.20013.

Shi, X., R. T. McNider, M. P. Singh, D. E. England, M. J. Friedman, W. M. Lapenta, and W. B. Norris, 2005: On the behavior of the stable boundary layer and the role of initial conditions. *Pure Appl. Geophys.*, **162**, 1811–1829, doi:10.1007/s00024-005-2694-7.

Sorbjan, Z., 2010: Gradient-based scales and similarity laws in the stable boundary layer. *Quart. J. Roy. Meteor. Soc.*, **136**, 1243–1254, doi:10.1002/qj.638.

Steeneveld, G. J., B. J. H. van de Wiel, and A. A. M. Holtslag, 2006: Modeling the evolution of the atmospheric boundary layer coupled to the land surface for three contrasting nights in CASES-99. *J. Atmos. Sci.*, **63**, 920–935, doi:10.1175/JAS3654.1.

Sun, J., and Coauthors, 2004: Atmospheric disturbances that generate intermittent turbulence in nocturnal boundary layers. *Bound.-Layer Meteor.*, **110**, 255–279, doi:10.1023/A:1026097926169.

——, L. Mahrt, R. M. Banta, and Y. L. Pichugina, 2012: Turbulence regimes and turbulence intermittency in the stable boundary layer during CASES-99. *J. Atmos. Sci.*, **69**, 338–351, doi:10.1175/JAS-D-11-082.1.

——, D. H. Lenschow, M. A. LeMone, and L. Mahrt, 2016: The role of large-coherent-eddy transport in the atmospheric surface layer based on CASES-99 observations. *Bound.-Layer Meteor.*, **160**, 83–111, doi:10.1007/s10546-016-0134-0.

Svensson, G., and Coauthors, 2011: Evaluation of the diurnal cycle in the atmospheric boundary layer over land as represented by a variety of single-column models: The Second GABLS Experiment. *Bound.-Layer Meteor.*, **140**, 177–206, doi:10.1007/s10546-011-9611-7.

Tijm, A. B. C., A. J. van Delden, and A. A. M. Holtslag, 1999: The inland penetration of sea breezes. *Contrib. Atmos. Phys.*, **72**, 317–328.

van de Wiel, B. J. H., A. F. Moene, R. J. Ronda, H. A. R. de Bruin, and A. A. M. Holtslag, 2002a: Intermittent turbulence and oscillations in the stable boundary layer over land. Part II: A system dynamics approach. *J. Atmos. Sci.*, **59**, 2567–2581, doi:10.1175/1520-0469(2002)059<2567:ITAOIT>2.0.CO;2.

——, R. J. Ronda, A. F. Moene, H. A. R. de Bruin, and A. A. M. Holtslag, 2002b: Intermittent turbulence and oscillations in the stable boundary layer over land. Part I: A bulk model. *J. Atmos. Sci.*, **59**, 942–958, doi:10.1175/1520-0469(2002)059<0942:ITAOIT>2.0.CO;2.

——, A. F. Moene, and H. J. J. Jonker, 2012a: The cessation of continuous turbulence as precursor of the very stable nocturnal boundary layer. *J. Atmos. Sci.*, **69**, 3097–3115, doi:10.1175/JAS-D-12-064.1.

——, ——, ——, P. Baas, S. Basu, J. M. M. Donda, J. Sun, and A. A. M. Holtslag, 2012b: The minimum wind speed for sustainable turbulence in the nocturnal boundary layer. *J. Atmos. Sci.*, **69**, 3116–3127, https://doi.org/10.1175/JAS-D-12-0107.1.

——, and Coauthors, 2017: Regime transitions in near-surface temperature inversions: A conceptual model. *J. Atmos. Sci.*, **74**, 1057–1073, doi:10.1175/JAS-D-16-0180.1.

van Hooijdonk, I. G. S., J. M. M. Donda, H. J. H. Clercx, F. C. Bosveld, and B. J. H. van de Wiel, 2015: Shear capacity as prognostic for nocturnal boundary layer regimes. *J. Atmos. Sci.*, **72**, 1518–1532, doi:10.1175/JAS-D-14-0140.1.

van Ulden, A. P., and J. Wieringa, 1996: Atmospheric boundary layer research at Cabauw. *Bound.-Layer Meteor.*, **78**, 39–69, doi:10.1007/BF00122486.

Vignon, E., and Coauthors, 2017: Stable boundary layer regimes at Dome C, Antarctica: Observation and analysis. *Quart. J. Roy. Meteor. Soc.*, **143**, 1241–1253, doi:10.1002/qj.2998.

Whiteman, C. D., T. Haiden, B. Pospichal, S. Eisenbach, and R. Steinacker, 2004: Minimum temperatures, diurnal temperature ranges, and temperature inversions in limestone sinkholes of different sizes and shapes. *J. Appl. Meteor. Climatol.*, **43**, 1224–1236, doi:10.1175/1520-0450(2004)043<1224:MTDTRA>2.0.CO;2.

Wyngaard, J. C., 1973: On surface-layer turbulence. *Workshop on Micrometeorology*, D. A. Haugen, Ed., Amer. Meteor. Soc., 101–149.

Zhou, B., and F. K. Chow, 2014: Nested large-eddy simulations of the intermittently turbulent stable atmospheric boundary layer over real terrain. *J. Atmos. Sci.*, **71**, 1021–1039, doi:10.1175/JAS-D-13-0168.1.

Zilitinkevich, S. S., T. Elperin, N. Kleeorin, I. Rogachevskii, I. Esau, T. Mauritsen, and M. W. Miles, 2008: Turbulence energetics in stably stratified geophysical flows: Strong and weak mixing regimes. *Quart. J. Roy. Meteor. Soc.*, **134**, 793–799, doi:10.1002/qj.264.